

Inclusion Formation in Self-Shielded Flux Cored Arc Welds

An investigation was made to see whether the same analytical models used to predict oxide inclusion in weld metal can also be used to predict nitride formations

BY M. A. QUINTANA, J. McLANE, S. S. BABU AND S. A. DAVID

ABSTRACT. Nonmetallic inclusions in two weld metals were characterized with respect to variations in weld aluminum concentration. Two self-shielded flux cored arc welding (FCAW-S) electrodes were used to produce welds for optical, scanning and transmission electron microscopy. The inclusions in the weld with high-aluminum concentration were predominantly aluminum nitride. In contrast, the inclusions in welds with low-aluminum and high-titanium concentrations were mostly aluminum oxide and titanium carbonitrides. The measurements were compared with predictions from multiphase, multicomponent thermodynamic equilibrium calculations. The calculations agreed with the experimental measurements and predicted the formation of aluminum nitride in high-aluminum welds and also simultaneous formation of aluminum oxide and titanium carbonitrides. However, the predicted volume fractions were lower than experimental values.

Introduction

It is well known that nonmetallic inclusions play an important role in the evolution of microstructures in steel weld metals. They influence the partitioning of alloying elements between solid solution and second phases depending upon the temperature of the formation. Also, they may act as nucleation sites for solidification and solid-state transformations on cooling. Inclusions are also known to have a direct effect on mechanical prop-

erties. If present in sufficient numbers and size, inclusions may also influence the ductile-to-brittle Charpy transition by providing initiation sites for cleavage cracks and reduce upper-shelf energy.

Most of the documented work on inclusions in weld metal has focused on welding processes that shield the arc and molten metal from atmospheric contamination [*i.e.*, gas metal arc welding (GMAW), gas-shielded flux cored arc welding (FCAW-G), shielded metal arc welding (SMAW) and submerged arc welding (SAW)]. In conventional steel weld metals produced by these processes, the oxidizing atmosphere produced by the consumables and/or supplied by the shielding gas is accommodated by excess Mn and Si in the electrode, which effectively deoxidize the molten weld metal. Much of the deoxidation product "floats out," creating silicate islands on the surface of GMA welds and contributing to the slag layer in FCAW-G, SMAW and SAW. Historically, much experimental work was done to characterize the oxide inclusions in these systems in relation to the resulting microstructures and properties (Refs. 1-8). Recent advances in computational models and analytical tools make it possible, in some cases, to predict the deoxidation sequence and the oxide inclusion formation with reasonable accuracy

(Refs. 7-10). By contrast, relatively little effort has focused on weld metals in which nitride rather than oxide formation is dominant [*i.e.*, self-shielded flux cored arc welding (FCAW-S)] (Refs. 11-16). This work was undertaken to determine whether the same analytical techniques could be used to accurately predict inclusion formation in FCAW-S deposits.

Weld metal produced by FCAW-S is unique in that the welding process and consumables do not intentionally protect the molten metal from atmospheric contamination. Rather, such contamination is anticipated and necessitates the use of strong deoxidizers and denitrifiers to ensure deposition of sound weld deposits. Inclusion of these elements (*e.g.*, Al, Ti and Zr) results in weld metal chemical compositions that are significantly different from other conventional arc weld deposits in the same strength range. As illustrated in Table 1, FCAW-S deposits have higher aluminum and nitrogen in conjunction with lower oxygen than other conventional arc weld deposits. The alloy balance in terms of carbon and manganese levels may also differ in some cases, but the major differences are in the nitrogen and oxygen contents and the amount of excess deoxidizer/denitrifier remaining in the weld metal (Refs. 14, 15).

Experimental Approach

Two FCAW-S weld metal systems were selected for investigation, E70T-4 and E71T-8 (Ref. 17), which represent significantly different Al, O and N levels as well as alloy balance. Specifically, these electrodes represent the extremes of the typical aluminum range for FCAW-S deposits. Single V-groove welds were produced over steel backing using the joint geometry illustrated in Fig. 1.

The welding conditions summarized in Table 2 are within the manufacturer's recommended operating ranges for each

KEY WORDS

Self-Shielded Flux Cored
Oxide Inclusions
Nitride Inclusions
Nonmetallic Inclusions
Aluminum Oxide
Aluminum Nitride

M. A. QUINTANA is with The Lincoln Electric Co., Cleveland, Ohio. J. McLANE is with Eveready Battery Co., Cleveland, Ohio (formerly with The Lincoln Electric Co.). S. S. BABU and S. A. DAVID are with Oak Ridge National Laboratory, Oak Ridge, Tenn.

Paper presented at the AWS 80th Annual Meeting, April 12-15, 1999, St. Louis, Mo.

Table 1 — Weld Metal Chemical Composition Comparison (wt-%)

Element	SMAW E7018	FCAW-G E70T-1	FCAW-S E7XT-X
C	<0.08	0.03–0.08	<0.4
Mn	1.2–1.5	1.3–1.7	0.5–1.2
Si	0.2–0.5	0.6–0.9	0.2–0.5
Al	0.01	<0.2	0.5–1.8
N	<0.01	<0.01	~0.05
O	~0.040	~0.070	0.005–0.040

of the electrodes. All welding was accomplished in the flat (1G) position. The two welds were made with significantly different welding heat inputs necessitated by the respective electrode diameters and are representative of actual usage. It was not possible to obtain electrodes representing extremely high and extremely low aluminum levels in sizes that would permit welding with the same heat input. Although differences in the thermal cycle due to heat input influence inclusion formation (Ref. 18), the large differences in chemical composition are expected to overshadow the effect of different heat inputs.

Transverse macrosections were taken from each weld for the experimental work. Bulk weld metal chemical compositions were determined using a BAIRD Model DV 4 emission spectrometer and LECO analysis equipment. Samples for carbon, sulfur and aluminum analyses were taken by collecting chips after drilling at the same locations. Total aluminum content was determined by atomic absorption spectroscopy following dissolution in aqua regia/hydrogen fluoride and fuming in perchloric acid. Solid cylinders were removed from equivalent locations in adjacent sections for oxygen and nitrogen determinations.

Metallographic specimens were polished with the final step with a 1- μ m diamond and were examined without etching in a light microscope at magnifications up to 1000X. Subsequently, carbon-extraction replicas and thin foils were prepared for examination at higher magnifications. All metallographic sample preparation utilized standard techniques with one exception. Because the likelihood of aluminum nitride formation was considered high and aluminum nitride is known to be soluble in water and mild alkali, it was necessary to eliminate the use of all soap and water in the sample preparation. Accordingly, polished samples were rinsed in either reagent-grade methanol or toluene, and carbon-extraction replicas were rinsed in alcohol rather than water. Transmission electron microscopy (TEM) was accomplished using Philips CM-12 and Philips CM200T

Table 2 — Welding Conditions Used in This Investigation

	High-Aluminum E70T-4	Low-Aluminum E71T-8
Electrode diameter [in. (mm)]	0.120 (3)	0.078 (2.0)
Tip-to work distance [in (mm)]	2.75 (70)	0.75 (19)
Voltage	31–36	19–20
Amperage	525–590	270–280
Wire feed rate [in./min (mm/s)]	225–250 (95–106)	120 (51)
Heat input [kJ/in. (kJ/mm)]	86–98 (3.4–3.8)	54–58 (2.1–2.3)
Preheat	ambient	ambient
Interpass (see note) [°C (°F)]	163 (325) max.	163 (325) max.

Note: Test welds heat quickly, reaching maximum interpass temperature in 1–2 passes. Thereafter, interpass temperature was maintained at 150–163 °C (300–325°F) through completion of the test welds.

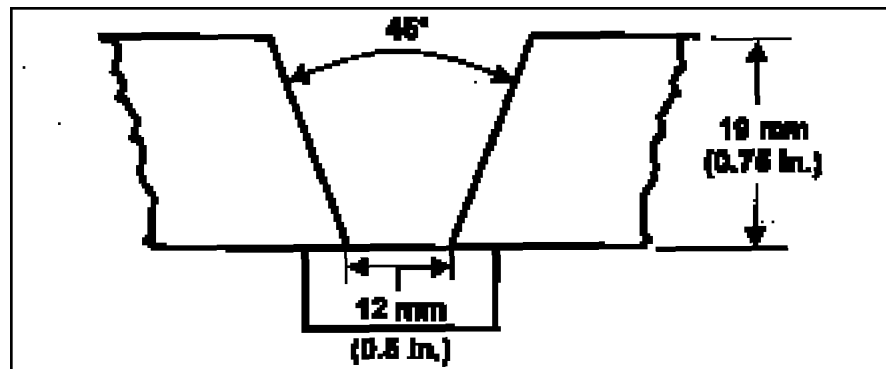


Fig. 1 — Weld joint geometry.

equipped with light element energy-dispersive X-ray (EDS) analysis capability. Scanning electron microscopy was accomplished using a JEOL 5800 and an Amray 1645 with light element EDS.

Chemical compositions of inclusions were determined semiquantitatively using EDS in both SEM and TEM. Inclusion number density, size distribution and volume fractions were determined using SEM images from the Amray at 5000X. Data from ten randomly selected frames for each weld deposit were collected, resulting in a sample size of about 4300 square μ m, 265 particles for the high-aluminum case and 492 particles for the low-aluminum case. The SEM images from extraction replicas made it possible to determine the inclusion size and shape more accurately than would have been possible with just the polished cross sections. Image analysis software was used to collect statistics on what amounted to two-dimensional projections of three-dimensional particles with relatively complex geometric configurations. In conventional C-Mn weld metal systems that produce generally spherical particles, it is customary to compile inclusion statistics based on diameter. Because of the more complex shapes en-

countered in the two FCAW-S systems considered here, the maximum dimensions and equivalent diameters were considered more relevant. “Equivalent diameter” is the diameter of a circle of a size equivalent to the area of complex shape. Consequently, inclusion volume was determined by calculating the volume of an equivalent sphere. The total area sampled for each weld multiplied by the respective mean equivalent inclusion diameter was considered a reasonable estimate of the volume of material sampled. Volume fractions were estimated by dividing total inclusion volume by sample volume.

Thermodynamic Calculations

Thermodynamic equilibrium among various oxides, nitrides and liquid steel was calculated using version L of ThermoCalc™ software (Ref. 19). The calculations considered the elements Fe, Al, C, Mn, Si, Al, Ti, O and N and the following phases: liquid, -ferrite, austenite, cementite, Al_2O_3 , $MnOAl_2O_3$, TiO , TiO_2 , Ti_2O_3 , Ti_3O_5 , $MnOTiO_2$, SiO_2 , MnO , SiO_2 , MnO , AlN and $Ti(CN)$. In order to estimate chemical compositions, volume fractions and initial temperatures of for-

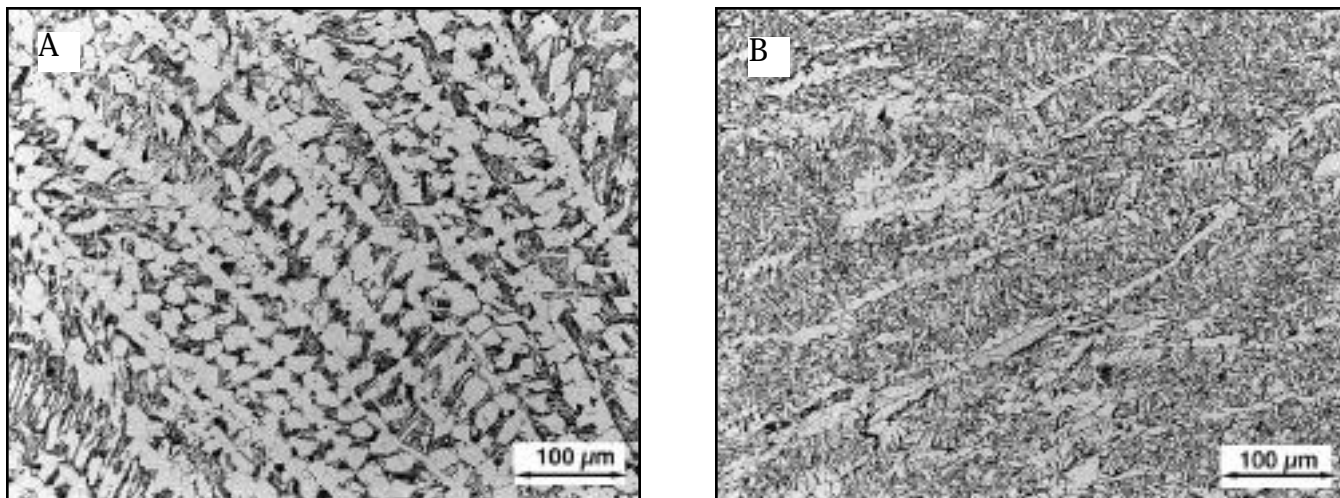


Fig. 2 — Optical micrographs of the as-welded microstructure. A — High-aluminum weld deposit (E70T-4); B — low-aluminum weld deposit (E71T-8).

Table 3 — Chemical Test Summary

Weld	C	S	P	Mn	Si	Al	Ni	Ti	O	N
High-aluminum E70T-4	0.234	<0.003	0.011	0.50	0.28	1.70	0.02	0.003	0.006	0.064
Low-aluminum E71T-8	0.149	<0.003	0.005	0.64	0.30	0.53	0.01	0.058	0.030	0.033

mation of the nonmetallic phases in each of the two weld metal systems were calculated at a temperature just before solidification. It was assumed the chemical composition of the molten pool at this temperature could be approximated by the final weld deposit composition. While calculating the volume fraction of oxides and nitrides, the compounds that formed during cooling from initial temperature of formation to 1527°C (~ melting point of the welds) were added together. Moreover, the changes in liquid composition due to the formation of these compounds were also considered using Scheil assumptions. Further details about such calculations can be found in Ref. 20.

Results and Discussion

The chemical test results for the two FCAW-S deposits are summarized in Table 3. In the high-aluminum case, the E70T-4 electrode produced weld metal aluminum at 1.70 wt-% with oxygen and nitrogen levels of 60- and 640-wt ppm, respectively. The low-aluminum weld metal produced with the E71T-8 electrode had far less aluminum at 0.53% by weight with oxygen and nitrogen levels of 300- and 330-wt ppm, respectively. Also, the presence of 0.058 wt-% titanium in the low-aluminum deposit indicates the use of a second deoxidizer/denitrider in the E71T-8 electrode. While the evolution of microstructures

in these two weld metals is discussed in detail elsewhere (Ref. 21), the optical micrographs of as-welded microstructure from both weld deposits are presented in Fig. 2 to supplement the inclusion comparisons. It is apparent that the differences in chemical composition affect more than the inclusion formation. The micrographs show a large fraction of columnar skeletal ferrite morphology in high-aluminum welds. The presence of ferrite is attributed to the sluggish austenite formation in these welds during weld cooling. The sluggish austenite formation is related to the increase in the stability of ferrite, owing to a large concentration of aluminum in solid solution. In contrast, the low-aluminum weld showed classic ferrite morphology, which formed from decomposition of austenite. These observations are consistent with earlier work by Kotecki (Refs. 15, 16).

Thermodynamic Predictions

High-Aluminum Deposit (E70T-4)

In the case of the E70T-4 deposit, the ThermoCalc™ predictions favored the formation of AlN over Al₂O₃ or Ti(CN). Fig. 3A shows the volume fraction of AlN as a function of temperature while cooling. The initiation of AlN formation from liquid steel was predicted to occur at 1666°C. No other nonmetallic phases

were predicted to form.

To evaluate the relative stability of oxides and nitrides in this weld metal system, the stability diagrams for liquid steel in equilibrium with Al₂O₃, AlN or Ti(CN) were calculated at 1527°C and are shown in Fig. 3B. This calculation is consistent with multicomponent, but was limited to two phases at a time. The nominal concentrations of Al, O, Ti and N of the weld metal are also shown in the diagram. The calculations clearly show that for this weld metal only AlN will form. However, the stability diagram also shows some interesting features. The formation of Al₂O₃ is predicted to occur only below certain Al and O concentrations, and an inadvertent increase in Al will not promote Al₂O₃ formation. This complex stability of Al₂O₃ is attributed to the interaction energies of Al and O in liquid steel. The stability diagrams also show minimum concentrations of Al, Ti and N are needed for the initiation of AlN and/or Ti(CN) phases in the liquid.

The above calculations considered each phase in isolation. However, it is desirable to evaluate the competition between each phase as a function of one or more alloying element concentrations. Therefore, the calculations were extended to predict the volume fraction of various phases as a function of aluminum concentration only in Fig. 3C at 1527°C. The calculations are consistent with multicomponent, multiphase equilibrium. The calculations indicated that below ~0.5 wt-% Al concentration, the formation of AlN will cease and Al₂O₃ formation will be favored while other elemental concentrations remain constant.

Low-Aluminum Deposit (E71T-8)

Similar calculations were performed

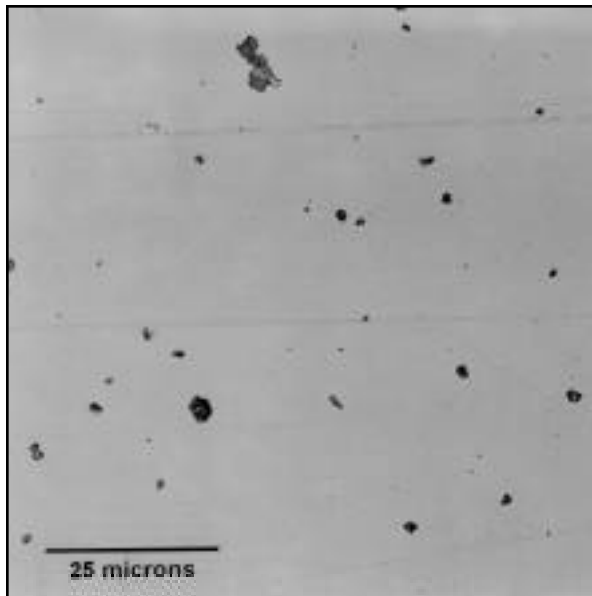


Fig. 5 — Optical micrograph of unetched high-aluminum weld (E70T-4).



Fig. 6 — SEM micrograph of high-aluminum weld (E70T-4).

Fig. 3B. This is attributed to the interaction energies between dissolved titanium, nitrogen and oxygen. It is noteworthy that even the formation of Al_2O_3 is very close to the stability line and that a small change in aluminum concentration can eliminate the Al_2O_3 formation, favoring only $\text{Ti}(\text{CN})$ formation.

Calculations were extended to predict the volume fractions of various phases as functions of aluminum concentration, considering all the phases at 1527°C — Fig. 4C. Some interesting features can be observed in this calculation. At very low levels of aluminum, the calculations predicted the formation of Ti_2O_3 . With an increase in aluminum the volume fraction of Al_2O_3 increases. However, at 0.7 wt-% aluminum the formation of Al_2O_3 ceases. The formation of aluminum nitride starts only above 2 wt-%. This interval of the absence of aluminum reaction is an interesting observation, and further work is needed to evaluate this composition experimentally. Interestingly, the formation of $\text{Ti}(\text{CN})$ was found to occur in all aluminum concentrations, which needs to be evaluated with future experiments.

Microstructural Observations

High-Aluminum Deposit (E70T-4)

Initial microscopic examination revealed a relatively uniform distribution of coarse, faceted particles, many with complex shapes, as illustrated in Fig. 5. On closer examination at higher magnifications, the complex shapes were actually large agglomerations (Fig. 6) of

Table 4 — Inclusion Summary Statistics

Weld	Mean Equivalent Diameter, $d_{\text{mean}}, \mu\text{m}$	Maximum Equivalent Diameter, $d_{\text{max}}, \mu\text{m}$	Max. Dimension, μm	Number Density (N), m^{-3}	Volume Fraction ^(a)	Elemental Composition
High-aluminum E70T-4	0.93	5.0	8.5	6.627×10^{16}	0.0279	Al, N some Fe
Low-aluminum E71T-8	0.37	2.5	4.0	3.092×10^{17}	0.0080	Al, O Ti, N

^(a) Estimated volume fraction = $N \cdot (4/3) \cdot \pi \cdot (d_{\text{mean}}/2)^3$

smaller particles (Fig. 7). EDS verified the presence of Al and N in the inclusions (Fig. 7C), indicating that they are, indeed, aluminum nitride and supported the predictions from thermodynamic calculations. It is important to note that no experimental evidence was found for aluminum oxide formation in this weld. The large agglomerations and the relatively uniform distribution of smaller particles suggest initial formation of these inclusions in the liquid prior to the start of solidification. This is consistent with a predicted inclusion-formation start temperature above the liquidus — Fig. 3A. In addition, the AlN inclusions were highly faceted — Figs. 6, 7.

It was apparent from detailed TEM observations of the Fe-rich cores found in some of the smaller discrete particles that the aluminum nitrides had nucleated heterogeneously — Fig. 8. Specific identification of these Fe-rich particles proved to be rather difficult. They were first observed in the TEM images of the very small inclusions in the carbon extraction replicas, appearing as dark spots near the

centers of the hexagonal inclusions — Fig. 8A. EDS indicated strong Fe peaks associated with these particles, which were absent at the inclusion perimeters — Fig. 8B. EDS in the SEM indicated the presence only of aluminum and nitrogen. No Fe-rich phases were found on the exterior surfaces of the inclusions, suggesting the Fe-rich particles observed by the TEM were internal, serving as heterogeneous nucleation sites. Although the presence of Fe in the nitride inclusions was not predicted, it is consistent with other reported results (Ref. 11). Because the formation of iron compounds was not anticipated for either of the two weld metal systems under consideration, it was not included in the thermodynamic analysis, which considered only the oxides and nitrides of aluminum and titanium. Therefore, these Fe-rich particles are assumed to be the unmelted Fe-rich compounds. Further work is needed to understand the formation of these compounds during self-shielded flux-cored arc welding.

Simple statistical analysis of the in-

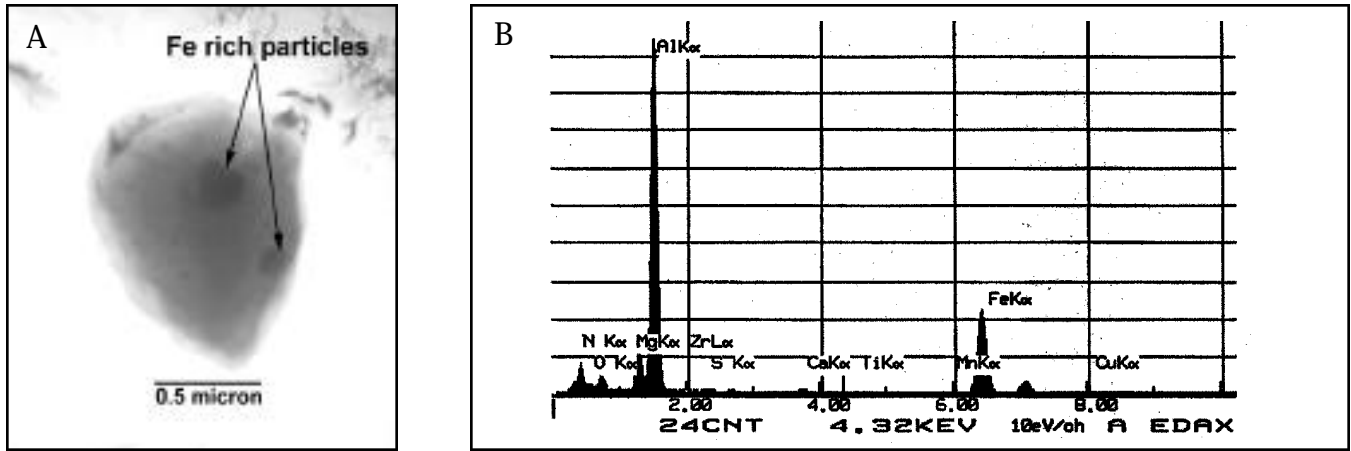


Fig. 8 — A — High-aluminum weld (E70T-4), AlN with Fe-rich areas; B — EDS spectrum obtained from Fe-rich areas.

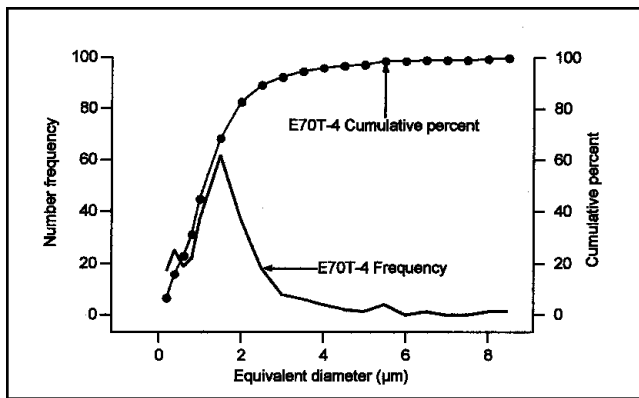


Fig. 9 — Inclusion size distributions from high-aluminum weld.

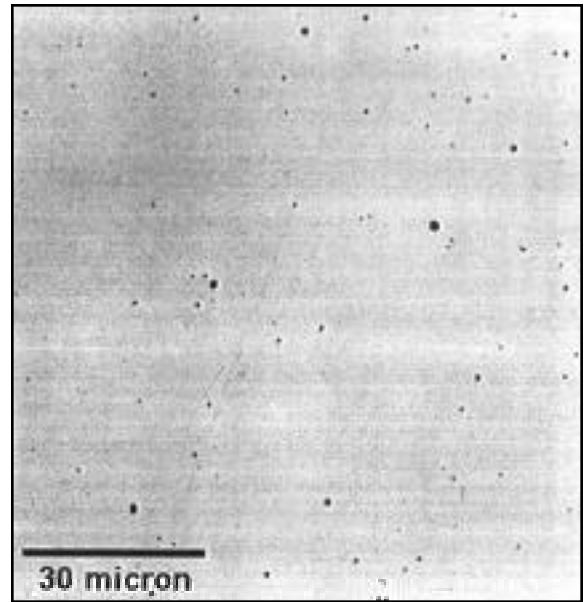


Fig. 10 — Typical inclusions of low-aluminum weld (E71T-8).

state. However, thermodynamic predictions agree with the trends observed in the experimental data.

From the results presented above, it is apparent thermodynamic calculations agree reasonably well with the experimentally observed deoxidation and denitriding conditions in self-shielded flux cored arc welds. The calculations predict the formation of AlN in high-aluminum welds and the formation of Al_2O_3 and Ti(CN) in low-aluminum welds. The calculations predicted the expected trend of decreasing inclusion volume fraction in the low-aluminum weld compared with that of the high-aluminum weld. However, the calculations do not agree with the magnitudes of volume fractions.

The decision to neglect the influence of heat input and reaction kinetics does not explain the consistent underprediction of inclusion volume fraction. If anything, the nonequilibrium conditions prevalent during weld solidification are expected to lead to over prediction of inclusion volume fraction when predictions are based exclusively on thermodynamic equilibria. It is more likely the

errors in prediction arise because inclusion formation after solidification was not considered in the analysis. Further, any comparison of heat input variance between the two weld types studied would have little relevance considering the inclusions are of totally different chemical compositions.

Summary and Conclusions

The chemical constituents identified in the inclusions from both the E70T-4 and E71T-8 weld metals are consistent with the thermodynamic calculations. Although it was not possible to experimentally verify temperatures at which precipitation occurred, the agglomeration of inclusions in the E70T-4 weld metal was consistent with the prediction of initial formation in the liquid.

The calculations predicted chemical constituents with reasonable accuracy; however, the comparisons with experimental measurements of volume fraction were only fair. The iron-rich phases at the

centers of the aluminum nitride inclusions were not predicted because their formation was not anticipated and therefore were not included in the analysis. This oversight and inability to consider the inclusion formation at low temperature may have contributed to the fact that accurate thermodynamic estimates of inclusion volume fraction were not consistently obtained. Although the prediction for the low-aluminum weld is in fair agreement with experimental results, the prediction for the high-aluminum weld was not; volume fraction was underestimated by an order of magnitude.

These initial results are by no means complete; however, they suggest thermodynamic predictions can provide reasonable estimates of inclusion composition, if not volume fraction, in these FCAW-S

